X-ray tomographic reconstruction of macromolecular samples

Sandor Brockhauser,[a] Marco Di Michiel,[b] John E. McGeehan,[a] Andrew A. McCarthy[a] and Raimond B. G. Ravelli[a,c]*

[a]European Molecular Biology Laboratory (EMBL) Grenoble Outstation, 6 rue Jules Horowitz, 38042 Grenoble, France, [b]European Synchrotron Radiation Facility (ESRF), 6 rue Jules Horowitz, 38043 Grenoble, France, and [c]Leiden University Medical Center (LUMC), Einthovenweg 20, 2333 ZC Leiden, The Netherlands. Correspondence e-mail: ravelli@lumc.nl

The anomalous scattering properties of innate sulfur for proteins and phosphorus for DNA and RNA can be used to solve the phase problem in macromolecular crystallography (MX) *via* the single-wavelength anomalous dispersion method (SAD). However, this method, which is carried out at longer X-ray wavelengths (1.5–2.5 Å), is still not a routine tool in MX. The increased absorption from both air and sample associated with the use of longer X-ray wavelengths presents a key difficulty. The absorption can be corrected for through empirical algorithms, provided truly redundant data are available. Unfortunately, weakly diffracting macromolecular crystals suffer from radiation damage, resulting in a dose-dependent non-isomorphism which violates the assumption upon which these empirical algorithms are based. In this report, X-ray microtomography is used to reconstruct the three-dimensional shapes of vitrified macromolecular crystals including the surrounding solvent and sample holder. The setup can be integrated within an MX beamline environment and exploits both absorption and phase contrast. The dose needed for the tomographic measurements could be low enough to allow the technique to be used for crystal integrity characterization and alignment. X-ray tomography has some major benefits compared with the optical-light-based crystal alignment protocols currently used.

1. Introduction

In the absence of air absorption and material surrounding the crystal, absorption-corrected Bragg intensities are given by $I_{corr} = I_{meas}/A$, with

$$A = (1/V) \int_V \exp[-\mu(t_0 + t_1)] \, d^3t, \qquad (1)$$

where μ is the linear absorption coefficient of the crystal, t_0 is the incident-beam path length to each crystal volume element d^3t, t_1 is the scattered beam path length and the integration is carried out over the volume of the crystal V that is exposed to the X-ray beam. Extra corrections are needed to take the absorption of air and possibly the sample holder or surrounding liquid into account.

Absorption corrections have been used for decades, in particular for neutron and small-molecule X-ray crystallography. Classical methods require a precise description of the crystal geometry, which can be determined, for example, by measuring the bounding planes of a crystal through a microscope (Alcock, 1970; Ward & Caughlan, 1971). By operating an X-ray tube at very low voltage, soft X-rays are produced that can be used for taking a series of silhouette photographs, as shown by Tichý (1970). More than 25 years

later, Izumi *et al.* (1996) used a CCD camera and computerized tomography to reconstruct the crystal shape of an inorganic crystal, using parallel backlight illumination instead of soft X-rays. In order to overcome the problem of computation costs associated with numerical integration, more efficient protocols have been introduced (Coppens *et al.*, 1965), such as those based on Howells polyhedrons (Alcock *et al.*, 1972; Alcock, 1974; Clark, 1993). Further simplifications can be obtained for standard types of sample geometries, such as cylinders and cuboids (Langan *et al.*, 1995).

Macromolecular crystallography (MX) demanded a different approach. In the days prior to cryovitrification, crystals were typically enclosed in thin-walled glass capillaries (DeTitta, 1985). An undetermined amount of mother liquor would hold the crystal in place to prevent it from drying. Nowadays, an undefined volume of cryoprotectant buffer is used to hold the macromolecular crystal within a nylon or Kapton loop prior to vitrification and data collection at cryotemperatures (100 K). There is a perception that it is too involved to describe accurately all the elements of the absorption process, particularly the liquor surrounding the crystal. Instead, semi-empirical methods have been developed, such as azimuthal scans. This method, designed for an auto-

research papers

mated four-circle diffractometer, exploits the changes in intensity of X-ray reflections as a function of rotation ψ around the normal to their reflecting planes (North *et al.*, 1968; Kopfmann & Huber, 1968; Huber & Kopfmann, 1969; Flack, 1974, 1975; Schwarzenbach & Flack, 1989). For synchrotron measurements, Helliwell *et al.* (1984) proposed the measurement of protein crystal absorption surfaces by monitoring both the incident and the transmitted intensities. Programs were written to calculate an empirical absorption correction based on the minimization of the differences between $|F_{obs}^2|$ and $|F_{calc}^2|$ (Walker & Stuart, 1983; Parkin *et al.*, 1995). Absorption effects could also be corrected for by using an entirely empirical function which minimizes the differences between symmetry-equivalent reflections, as systematic errors due to absorption will not be evenly distributed through reciprocal space (Stuart & Walker, 1979; Messerschmidt *et al.*, 1990). In fact, most scaling programs used in the field of macromolecular crystallography today employ the latter method to correct simultaneously for anisotropic absorption, crystal decay and beam inhomogeneities (Kabsch, 1988; Blessing, 1995; Sheldrick, 1996; Otwinowski *et al.*, 2003; Evans, 2006). The success of these programs together with the tremendous improvements in instrumentation have resulted in a constant push to exploit weak anomalous signals for phasing (Wang *et al.*, 2006), which sometimes requires extensive tuning of the scaling parameters (Mueller-Dieckmann *et al.*, 2004). A multi-parametric scaling of diffraction intensities can include all known instrumental and data-collection parameters (Otwinowski *et al.*, 2003), but has to overcome the problem of highly correlated parameters. The use of realistic restraints could help in this.

The vast majority of MX data sets are now collected at modern synchrotron beamlines. Powerful undulator X-ray beams combined with fast-readout detectors allow complete data sets to be acquired in a matter of minutes. However, even at cryotemperatures, radiation damage will be noticeable at synchrotron wiggler and undulator beamlines, preventing the collection of highly redundant data to the desired resolution. Even when the same reflection has been measured multiple times, significant differences can be observed because of radiation damage. Scaling programs account for global changes, such as the overall resolution-dependent decrease of intensity. However, they cannot properly model the gradual increase in non-isomorphism caused by the X-ray beam (Ravelli & McSweeney, 2000; Weik *et al.*, 2000; Ravelli & Garman, 2006). Instead, because of the correlation of many scaling parameters, cosmetically improved radiation-damage-impaired data sets are obtained which still contain significant systematic errors. Better scaling restraints as well as improved models for X-ray-induced non-isomorphism might help to overcome this problem.

In this paper, we report the use of X-ray microtomography to determine the three-dimensional shape of a crystal within its surrounding liquid and sample holder. First, the principles of tomography are described [analogous to Cloetens (1999) and Weitkamp (2002)], introducing concepts such as the Radon transform, sinogram, Fourier slice theorem and filtered

backprojection to the macromolecular crystallographer. A general description of the interaction of X-rays with matter is given and the complex refractive index is introduced. A number of assumptions are made, such as the use of X-ray energies far from absorption edges. Although both absorption contrast and phase contrast are defined, we refer to Cloetens *et al.* (2006), Cloetens (1999) and Weitkamp (2002) for the quantitative treatment of phase contrast; here we only show that phase contrast leads to a sample–detector distance-dependent edge enhancement. We present simulations of the absorption of macromolecular crystalline samples at different energies and compare them with the absorption of the surrounding liquid. The X-ray beam will be not only absorbed by the crystalline sample but also attenuated because of Bragg diffraction (Murray *et al.*, 2004). This effect is discussed rather than described mathematically.

The X-ray microtomographic data that are presented here have been obtained at two different synchrotron undulator beamlines. Some data were obtained at a high-energy imaging beamline, showing superior reconstructions and clear phase contrast, whereas the absorption of the samples was minimal at the energies used. The tomography setup has been extended to operate in a standard macromolecular crystallography beamline environment. We describe how X-ray microtomography could aid analytical absorption corrections and discuss the prospects for using the technique for locating crystals within their sample holder, as well as cracks and other problematic regions within a crystal.

2. Theory

2.1. Tomography

The complex refractive index n is defined so that the wavenumber $k = 2\pi/\lambda$ in vacuum and the wavenumber in the material k' are related by $k' = nk$:

$$n = 1 - \delta + i\beta, \tag{2}$$

where δ is the refractive index decrement, β is the absorption index and λ is the wavelength of the X-ray beam. It is assumed that the interaction of a wave with the object is fully described by n, and consequently diffraction from a crystalline structure is neglected. A plane wave traveling through a sample in the direction **z** is of the form $\exp(inkz) = \exp[i(1 - \delta)kz] \times \exp(-\beta kz)$, where δ results in a phase shift and β results in absorption. The absorption index β is linked to the linear absorption coefficient μ by

$$\mu = (4\pi/\lambda)\beta. \tag{3}$$

For X-ray energies far from absorption edges, the refractive index decrement can be expressed as

$$\delta = \frac{r_c \lambda^2}{2\pi V} \sum (Z_j + f_j'), \tag{4}$$

where r_c is the classical electron radius (2.8 fm), V is the volume of the sample, the summation is over all the atoms within V, Z_j is the number of electrons of each atom and f_j' is the real part of the wavelength-dependent dispersion coeffi-

cient. If the dispersion correction is neglected (Cloetens, 1999), the above equation can be approximated to

$$\delta \simeq 1.3 \times 10^{-6} \rho \lambda^2, \qquad (5)$$

with the density ρ in g cm^{-3} and λ in Å. The interaction of X-rays with matter is thus very weak, $|1 - n| \simeq 10^{-6}$, and the propagation inside the sample can be assumed to be straight. It is therefore possible to project the object onto a single plane perpendicular to the propagation direction. An incident wave $u_{inc}(x, y)$ will relate to $u_o(x, y)$, the wave downstream of the object, through the transmission function of the object $T(x, y)$:

$$u_o(x, y) = T(x, y) u_{inc}(x, y). \qquad (6)$$

The transmission function depends on the projection of the refractive index distribution through

$$T(x, y) = A(x, y) \exp[i\varphi(x, y)], \qquad (7)$$

with the amplitude $A(x, y) = \exp[-B(x, y)]$ and $B(x, y) = (2\pi/\lambda) \int \beta(x, y, z) \, dz$, and the phase modulation $\varphi(x, y) = (2\pi/\lambda) \int [1 - \delta(x, y, z)] \, dz$, where the integrations are carried out over the thickness of the object l in the propagation direction $\mathbf{z}$.

For an ideal detector with linear response and infinite resolution, the recorded intensity would be proportional to the squared modulus of the wave at the detector, $I_d(x, y) = |u_d(x, y)|^2$. At the exit of the sample ($d = z = l$), one obtains

$$I_0(x, y) = A^2(x, y) |u_{inc}(x, y)|^2 = A^2(x, y) I_{inc}(x, y). \qquad (8)$$

The amplitude A of the transmission function T can be obtained if the incident intensity $I_{inc}(x, y)$ is independently measured. It is related to the projection of the absorption coefficient μ:

$$\int \mu(x_0, y_0, z_0) \, dz = -\ln[I_0(x, y)/I_{inc}(x, y)]. \qquad (9)$$

At distances $d > l$, the phase modulation turns into amplitude information through propagation, giving rise to phase contrast that is proportional to the Laplacian of the decrement of the refractive index δ in the sample (Cloetens, 1999; Weitkamp, 2002).

In order to obtain a three-dimensional image, the object is viewed employing a large number of incidence angles. Radon (1917) showed theoretically that it is possible to reconstruct an object from its projections at different angles. In our case the relevant function is the complex refractive index $n(x, y, z)$. Let us rotate the object around the y axis and record two-dimensional images at multiple angular positions ω. For a particular slice of $y = y_0$, the two-dimensional projection $R(\omega, s)$ of $n(x, y_0, z)$ is

$$R(\omega, s) = \int \int n(x, y_0, z) \delta(x \cos \omega + z \sin \omega - s) \, dx \, dz, \quad (10)$$

where $\delta()$ is the Dirac delta function (not to be confused with δ, the refractive index decrement), and the integral transform $R(\omega, s)$ consists of the integral of $n(x, y, z)$ over the set of all lines represented by $x \cos \omega + z \sin \omega = s$, where s is the shortest distance from the line to the origin and ω is the angle the line makes with the z axis. This set of projections is called the Radon transform of the distribution $n(x, y, z)$. It is suffi-

cient to acquire images over half a turn, as images at 180° apart are the mirror image of each other: $R(\omega + \pi, s) = R(\omega, -s)$. The Radon transform $R(\omega, s)$ is often called a sinogram, since the Radon transform of a number of small objects appears graphically as a number of blurred sine waves with different amplitudes and phases. The tomographic reconstruction consists of the determination of the three-dimensional distribution from the available projections, which means finding the inverse Radon transform.

At the exit of the sample ($z = l$), one can obtain normalized images that are a projection of the linear absorption coefficient μ [equation (9)]. From this set of images, obtained at different values of ω, one can reconstruct the sinograms $R[\mu](\omega, s)$ {which is equal to $R[n](\omega, s)$ at $z = l$}.

The function $\mu(x, y, z)$ can be reconstructed from a sinogram $R[\mu](\omega, s)$ following the Fourier slice theorem. The one-dimensional Fourier transform of $R(\omega, s)$ is

$$\tilde{R}(\omega, k_s) = \int \exp(-isk_s) R(\omega, s) \, ds, \qquad (11)$$

where k_s is the spatial frequency and the notation $\tilde{f}$ is used for the Fourier transform of f. Substituting the expression for $R(\omega, s)$ into the above equation and shifting the property of the Dirac delta function gives

$$\begin{aligned} \tilde{R}(\omega, k_s) &= \int \int \int \mu(x, y_0, z) \delta(x \cos \omega + z \sin \omega - s) \\ &\quad \times \exp(-isk_s) \, dx \, dz \, ds \\ &= \int \int \mu(x, y_0, z) \exp[-i(x \cos \omega + z \sin \omega) k_s] \, dx \, dz \\ &= \tilde{\mu}(k_s \cos \omega, k_s \sin \omega). \end{aligned} \qquad (12)$$

Thus the Fourier slice theorem shows that μ can be obtained by taking the two-dimensional inverse Fourier transform of the one-dimensional Fourier transform of the measured projections $R(\omega, s)$.

The two-dimensional inverse Fourier transform of $\tilde{\mu}(k_x, k_z)$ is

$$\mu(x, y_0, z) = (1/4\pi^2) \int \int \tilde{\mu}(k_x, k_z) \exp[i(xk_x + zk_z)] \, dk_x \, dk_z, \qquad (13)$$

or, in polar coordinates,

$$\begin{aligned} \mu(x, y_0, z) = (1/4\pi^2) \int \int \tilde{R}(\omega, k_s) \exp[ik_s(x \cos \omega + z \sin \omega)] \\ \times |k_s| \, dk_s \, d\omega. \end{aligned} \qquad (14)$$

The integral $\int \tilde{R}(\omega, k_s) |k_s| \, dk_s$ is called the filtered back-projection at angle ω. It compensates for the non-uniform sampling of the spatial frequencies in R. The filter $|k_s|$ is often referred to as the ideal ramp filter because it amplifies the high frequencies and consequently the high-frequency noise. In practice, a finite number of projections are recorded, and each projection is sampled with a finite pixel size, which limits the reconstruction to a maximum frequency. The problems of amplifying noisy and non-existent data can be overcome by the use of modified ramp filters such as those proposed by Kak & Slaney (1988).

2.2. Absorption of macromolecular crystals

The linear absorption coefficient μ is approximately proportional to the cube of the wavelength λ with a constant

of proportionality ~0.22 mm^{-1} Å^{-3} (Arndt, 1984). We have used the program *RADDOSE* (Murray *et al.*, 2004) to calculate the linear attenuation coefficient $\mu_{att}(\lambda)$ for a number of macromolecular crystals. The attenuation coefficient includes, at the energies we use in this paper, photoelectric absorption, Compton scattering and Rayleigh scattering. The photoelectric effect is the largest contributor to the absorption coefficient. The program estimates the unit-cell contents on the basis of the number of amino acids in the protein and the number of RNA or DNA bases present. The presence of non-CHNO atoms within the macromolecule and solvent can be specified explicitly. The program computes the fraction of the unit cell that consists of solvent and fills it with water as well as any additional solvent constituents specified by the user. The program has been adapted to calculate μ_{sol} for the mother liquor surrounding the crystal, assuming that the mother liquor has the same composition as the solvent within the crystal.

Fig. 1(*a*) shows the calculated $\mu_{att}(\lambda)$ *versus* λ^3 within the wavelength range $0.25 < \lambda < 2$ Å for a variety of macromolecular crystals, native and soaked with heavy atoms. Calculations were performed for some of the samples described by Murray *et al.* (2004), as well as for samples used for the tomography experiments described in the present paper. The proportionality constant varies for the native crystals between 0.27 and 0.50 mm^{-1} Å^{-3} for the heat shock protein DegP and DNA, respectively. This is higher than the value given by Arndt (1984), as non-CHNO atoms like sulfur and phosphorus were taken into account. Absorption edges appear for crystals soaked with heavy atoms, abruptly increasing the attenuation coefficient at energies above the K and L absorption edges. Very little attenuation will occur at low wavelengths, *e.g.* 0.032 mm^{-1} at 0.3 Å for native chicken hen egg white lysozyme (HEWL), which corresponds to 0.6% attenuation for a 200 µm-thick crystal. A 400 m*M* Ho soak would more than double the attenuation coefficient at this wavelength: 0.072 mm^{-1} corresponding to 1.4% attenuation for the same crystal thickness. At longer wavelengths, the attenuation can be very large; for example, μ_{att} at 1.77 Å equals 1.82 *versus* 3.02 mm^{-1} for native *versus* Ho-soaked lysozyme (see *Materials and methods* for exact soaking conditions), which corresponds for a 200 µm-thick crystal to an attenuation of 30 and 44%, respectively. At 1 Å wavelength, a typical native 100 µm-thick protein crystal would show around 3.5% attenuation, which should be enough to be detected by X-ray microtomography in the absence of phase contrast.

However, the attenuation contrast between a macromolecular crystal and its surrounding solvent will be minimal. Fig. 1(*b*) shows the contrast between crystal and solvent for the same macromolecules as shown in Fig. 1(*a*). This contrast is approximately, in the absence of heavy atoms, independent of wavelength. It is in general very small, and only shows clear deviations if heavy-atom soaks are used. Specific binding of heavy atoms to the macromolecule, or incorporation of the heavy atom directly into the macromolecule, increases the contrast, making the crystal more attenuating than the solvent. On the other hand, concentrated heavy-atom soaks of weak binders, such as sodium bromide soaks or derivatization with some of the gadolinium complexes (Murray *et al.*, 2004), could lead to an attenuation coefficient that is higher for the solvent than for the crystal. Phase contrast X-ray microtomography would be best suited to discriminate between a crystal and its surrounding solvent, especially in the absence of heavy atoms.

3. Materials and methods

3.1. High-energy X-ray tomography

Crystals from lysozyme (HEWL) in complex with holmium, kindly provided by Dr Jean Jakoncic, were grown using the microbatch method under paraffin oil in the presence of a
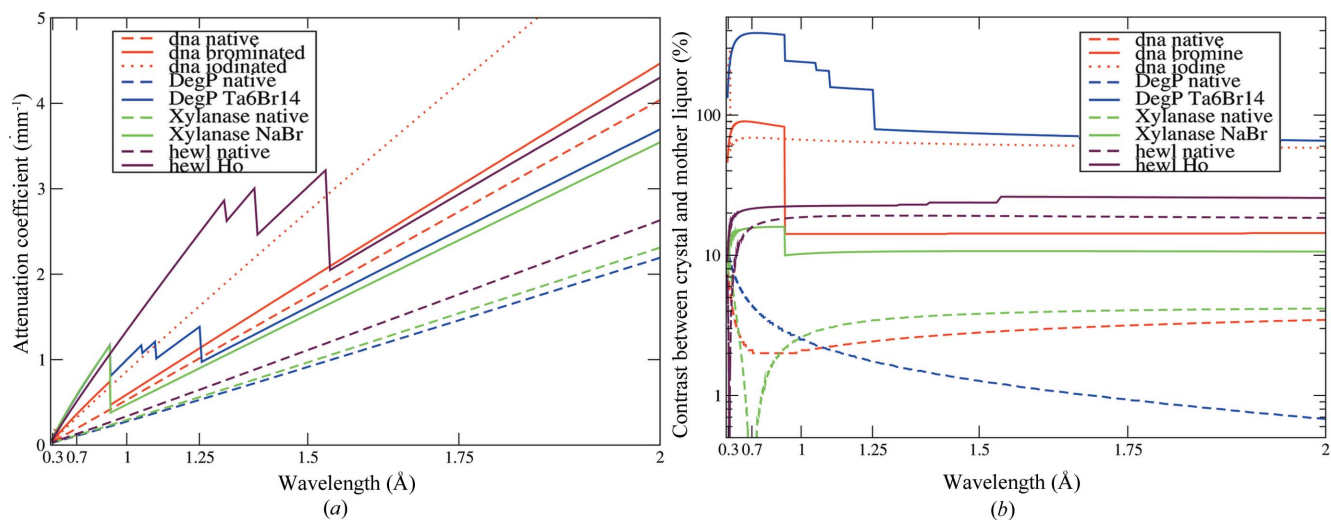

Figure 1
Crystal attenuation coefficient *versus* wavelength (*a*) and the contrast between the attenuation coefficient of a crystal *versus* its mother liquor (*b*). The *x* axis is linear with Å^3, but the numbers on the *x* axis directly correspond to the wavelength (Å). The calculations were performed using *RADDOSE* (Murray *et al.*, 2004) for the samples described in §3 [DNA and lysozyme (HEWL)], as well as two of the samples described by Murray *et al.* (2004): xylanase and the heat shock protein DegP, both for native crystals and soaks that were used for phasing.

0.2 M HoCl$_3$ solution and 25% glycerol (Jakoncic *et al.*, 2006). A large crystal (180 × 180 × 210 µm) was directly vitrified into a 100 K open-air cold nitrogen gas flow from an Oxford Cryostream 600 series.

The high-energy beamline ID15A at the European Synchrotron Radiation Facility (ESRF) was used to collect X-ray tomographic data. The synchrotron was operated in 2 times 1/3 fill mode. The filtered white high-energy X-ray beam (maximum flux at 55 keV) had a size at the sample of approximately 1 × 1 mm. Further details of the beamline and setup are given by Di Michiel *et al.* (2005).

A DALSTAR1M60 CCD camera coupled to a 10× magnification optics and to a LAG:Eu^{++} scintillator screen was used as detector. The sample was rotated by a vertical air bearing DC motor (Fig. 2a). The rotation axis was carefully aligned within an angular error of less than 2×10^{-3}° to be perpendicular to the X-ray beam and parallel to a row of detector pixels.

50 dark-signal images were recorded with the X-ray shutters closed, followed by 50 flatfield images, *i.e.* images of the beam profile without the sample in the beam. The 500 actual projection radiographs were recorded during a continuous 180° sweep of the sample around the rotation axis (Di Michiel *et al.*, 2005), using a total of 20 s of unattenuated X-ray beam.

The raw projection data were corrected for the dark signal, normalized to the beam profile without the sample (flatfield correction) and rearranged into sinograms. The position of the rotation axis was predetermined using images of reference tungsten wire (diameter 100 µm) by calculating the cross-correlation between the projection image at 0° and the position-reversed projection at 180°, and searching for its maximum while altering the vertical shift of both projections. The stack of tomograms were calculated using the ID15 *tomo* suite (Di Michiel *et al.*, 2005). A Kak and Slaney filter was used for the filtered backprojection, together with linear interpolation. The stack of reconstructions were imported into *VGStudio* (Volume Graphics, Germany) for three-dimen-

sional visualization, and objects were identified using histogram thresholding.

3.2. X-ray tomography on an MX beamline

Crystals of 16-*mer* 5′ GCTGGAAATTTCCAGC 3′ were grown as described by McGeehan *et al.* (2007). Brominated and iodinated derivates were synthesized by the incorporation of phosphoramidite 8-bromo-2′-deoxyguanosine at positions 5 and 15 or phosphoramidite 5-iodo-2′-deoxycytidine at positions 2 and 12. The native, brominated and iodinated DNA crystals were all grown under identical conditions using the hanging-drop vapour diffusion method combining 1 µl of 1 mM DNA plus 1 µl of reservoir solution over 1 ml of 34% PEG 200, 600 mM CaCl$_2$ and 10 mM HEPES pH 8.6. Crystals were vitrified directly into a 100 K open-flow cold nitrogen gas stream from an Oxford Cryostream 700 series without the need for further cryoprotection.

A FReLoN (fast readout, low noise) 2000 CCD camera was installed on the MX multiple-wavelength anomalous dispersion (MAD) beamline ID14-4 at the ESRF (Fig. 2b). A tenfold objective magnification was used, corresponding to an effective pixel size of 0.7 µm and a field of view of 1.4 × 1.4 mm for the 14 bit 2048 × 2048 pixel cooled CCD. The detector was mounted on a translation and rotation stage, and aligned to have its pixel rows parallel to the rotation axis. The latter belonged to the minidiffractometer MD2M, which forms, together with a slitbox and sample changer, the standard equipment of the ESRF MX beamlines (Beteva *et al.*, 2006; Cipriani *et al.*, 2006). The FreLoN camera could be translated along the beam direction towards the sample up to a minimum sample-to-scintillator distance of about 3 cm. Below this distance, the large scintillator holder would disturb the cryostream from the Oxford Cryostream 700 series and eventually collide with it.

The scintillation screen consisted of a 6 µm single-crystal layer of lutetium aluminium garnet doped with europium (LAG:Eu^{++}, Lu$_3$Al$_{4.4}$Sc$_{0.6}$O$_{12}$) and grown onto a 170 µm
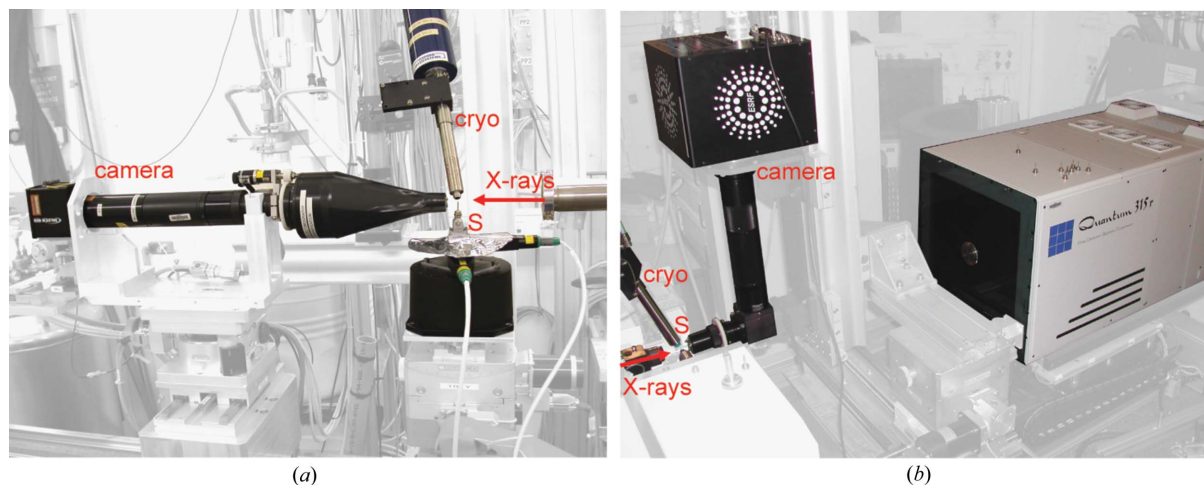

Figure 2
Microtomography setup on the high-energy X-ray beamline ID15A (*a*) and the MAD MX beamline ID14-4 (*b*). The X-ray beam direction (X-rays), camera position (camera), cryostream (cryo) and sample position (S) are marked.

yttrium aluminium garnet (YAG, $Y_3Al_5O_{12}$) substrate. The energy of the incoming beam was 12.7 keV (0.976 Å). The start- and stop-integration signal for the FReLoN CCD was triggered by the opening and closing of the fast piezo X-ray shutter.

50 dark-signal images were recorded with the X-ray shutters closed, followed by 50 flatfield images. The 360 actual projection radiographs were recorded in 0.5° steps, where additionally, in between each successive projection, an intermediate flatfield image was taken for which the crystal was translated out of the beam. After the collection of the projection radiographs, another series of 50 flatfield images was collected. The exposure time for each image was 0.15 s.

Beam-profile fluctuations made it necessary to collect a large series of intermediate flatfield images. A typical focal spot beamsize on ID14-4 is 250 µm FWHM vertically and 320 µm FWHM horizontally. In order to provide a larger field of view vertically, the beam was defocused by unbending the mirror (the horizontal field of view was limited both by the fixed curved radius of the mirror and the opening width of the piezo X-ray shutter). Unfortunately, the defocused beam showed clear vibrations linked to fluctuations in the mirror bending mechanism. The defocussing together with a long distance between the mirror and the sample aggravated the resulting shift of the beam profile impinging on the sample. Strong ring artifacts would be visible in the tomogram if the flatfield images taken prior to the collection of the projection radiographs had been solely relied upon (Weitkamp, 2002). These artifacts could be greatly reduced by the creation of a flatfield library, followed by automatic matching for each projection image to a set of best matching flatfield images.

Crystals of native, iodinated and brominated DNA were used for high-resolution microtomography experiments. For each crystal, two series of data were collected, one at minimal crystal-to-scintillator screen distance (3 cm) and one at a longer distance (9 cm). Flatfield correction was carried out as described above, and the tomographic reconstruction was performed using the *Image Processing Toolbox* from *Matlab* (MathWorks Inc., Natick, MA, USA) while applying the default ramp filter for frequency domain filtering and a spline interpolation in the backprojection. The program *Amira* from Mercury Computer Systems (Chelmsford, MA, USA) was used for three-dimensional visualization as well as for the determination of crystal, loop and solvent boundaries.

Figure 3
Flatfield-corrected projection image of an Ho-derivatized HEWL crystal collected on ID15A.
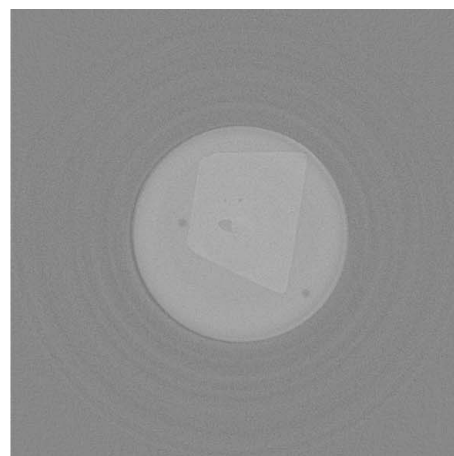
(a)
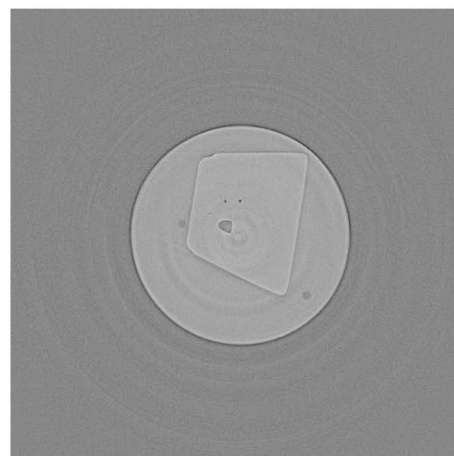
(b)
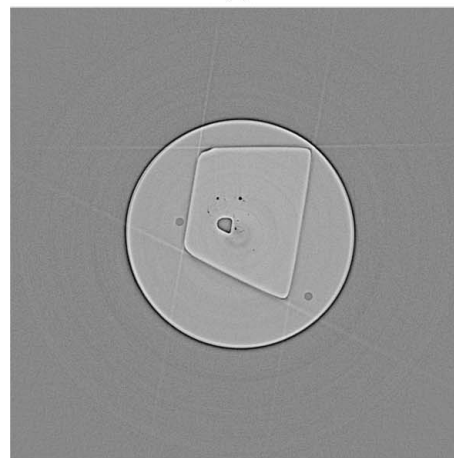
(c)

Figure 4
Reconstructed two-dimensional tomograms based on data collected at different crystal-to-detector distances [(a) 30 mm, (b) 100 mm and (c) 250 mm], showing the effect of increasing phase contrast.
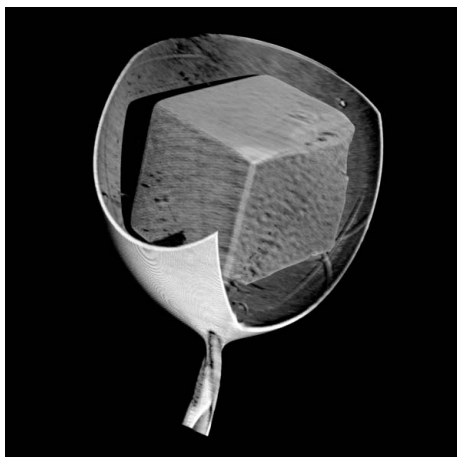
Figure 5
Full three-dimensional reconstruction of a vitrified lysozyme crystal and surrounding cryosolution as visualized with *VGStudio* (Volume Graphics, Germany). Objects were identified using histogram thresholding.

4. Results

Fig. 3 shows a flatfield-corrected projection image of the HEWL crystal collected on ID15A. The crystal is held in a loop that is mounted on a metal pin. The supporting pin is hollow, which can be clearly seen as the projection data were collected at relatively high X-ray energies (around 55 keV). The absorption contrast of the sample is very low; in fact, virtually no absorption contrast could be seen in projection radiographs that were collected on native crystals of ribonuclease and insulin (data not shown). In agreement with the calculations detailed in §2.2, some absorption contrast could be observed for the HEWL crystal as it was derivatized with

Ho. However, these images show clear phase contrast, which resulted in a sample–detector distance-dependent edge enhancement. Fig. 4 shows reconstructed slices of the HEWL crystal, based on projection images collected at increasing distance (30, 100 and 250 mm). The image taken at 250 mm reveals details such as the position of the nylon loops with 10 µm diameter and an imperfection within the bulk of the crystal. Both the crystal and the solvent boundaries are well defined; however, the straight crystal faces resulted in strong fringes that extend the image of the crystal and even its surrounding mother liquor. A full three-dimensional reconstruction was made based on the 250 mm projection series (Fig. 5). Histogram thresholding allowed the segmentation of the three-dimensional tomogram into crystal, surrounding solvent and loop.

Fig. 6 shows normalized projection images from the data collected on the MX beamline ID14-4. The contrast between the crystal and the solvent at 12.7 keV was calculated to be 2, 14 and 67% for native, brominated and iodinated DNA, respectively. Indeed, the largest contrast is observed for the iodinated DNA crystal. The brominated crystal should show a larger contrast with the solvent compared with the native crystal, but this is not so clear from Fig. 6. In fact, the amount of solvent surrounding these crystals is quite different, giving rise to varying projected absorption contrast between solvent and crystal. For example, the solvent layer becomes minimal between the loop and the native crystal (Fig. 7a), whereas the thickness of this layer gradually increases between the loop and the iodinated crystal (Fig. 7b). In all cases, very little absorption contrast was observed between the loop and the vitrified solvent. In contrast, clear phase contrast could be observed, especially at the envelope of the loop.
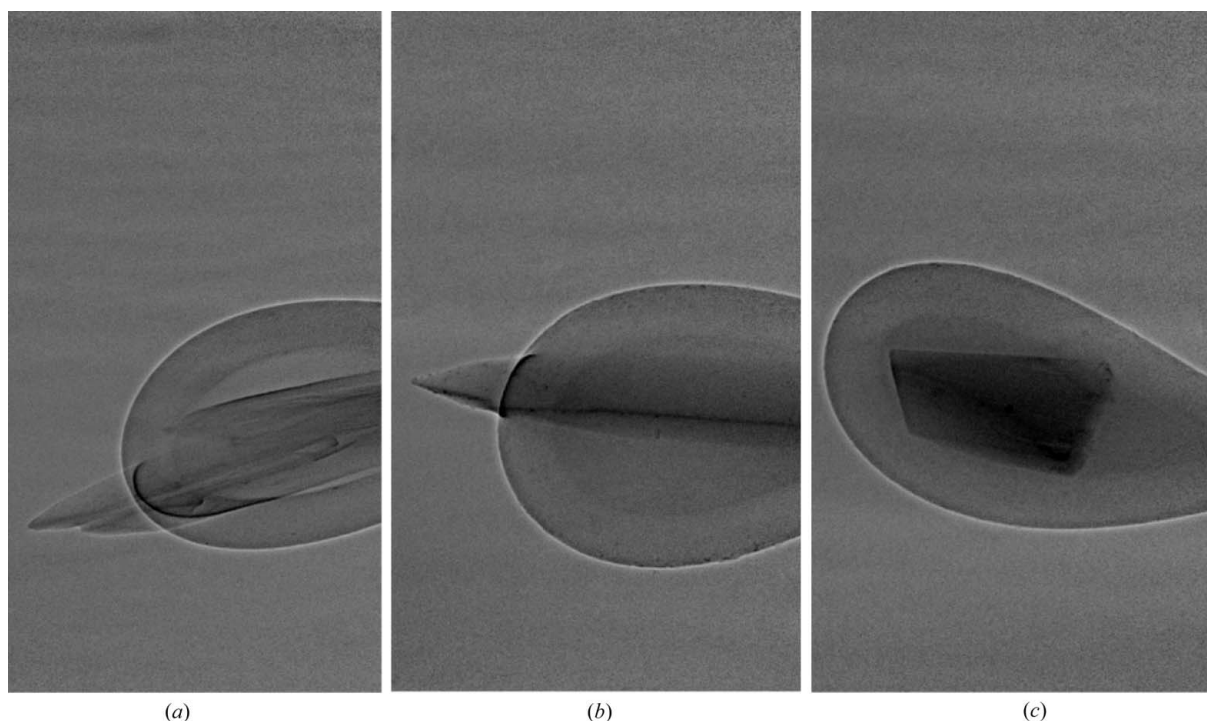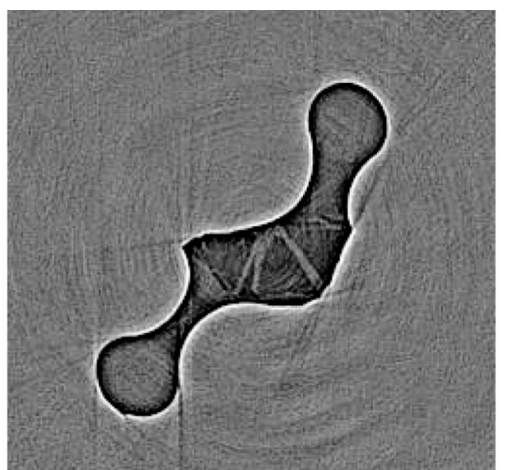

(a) (b) (c)

Figure 6
Flatfield-corrected projection images of native (a), brominated (b) and iodinated (c) DNA crystals, collected on the MX beamline ID14-4.

The tomographic data collected on the MX beamline were, in terms of artifacts, of inferior quality compared with those collected on the high-energy imaging beamline. This can be concluded from the inhomogeneous background on the normalized projection images (modulations in background intensity, Fig. 6) and the quality of the sinograms, as well as from the noise level in the final reconstructions. Nevertheless, all series contain significant details. Fig. 7 shows reconstructed slices of a native and an iodinated crystal, based on data collected on the MX beamline. It can be clearly seen that the native crystal actually consists of several triangular rods, separated by a few micrometres. Fig. 7(a) shows the cross section of three triangular rods, as well as splinters located in between the rods. Such details are virtually impossible to observe with visible light, even when using high-quality optics such as the on-axis viewer that is part of the micro-diffractometer (Lavault et al., 2006). The approximately three-pixel-wide (2 µm) crack that is visible for the iodinated crystal (Fig. 7b) starts from one end of the crystal and is about 14 µm long. The other end of the crystal also shows some cracks, extending for about 40 µm. One would expect that, for this crystal, the cleanest diffraction spots could be obtained while exposing the central 60 µm of the 115 µm-long crystal.

Fig. 8 shows the reconstructed native, brominated and iodinated crystals (purple), loops (yellow) and solvent (transparent pink) after analysis as obtained with Amira. The native crystalline sample was modelled as three individual crystals. Accurate modelling of additional details, such as cracks, splinters and connections, would require extensive

(a)

(b)

(c)

Figure 8
Three-dimensional reconstructed crystals (purple), loop (yellow) and solvent (transparent pink) for the vitrified brominated (a), native (b) and iodinated (c) samples collected on the MX beamline ID14-4.
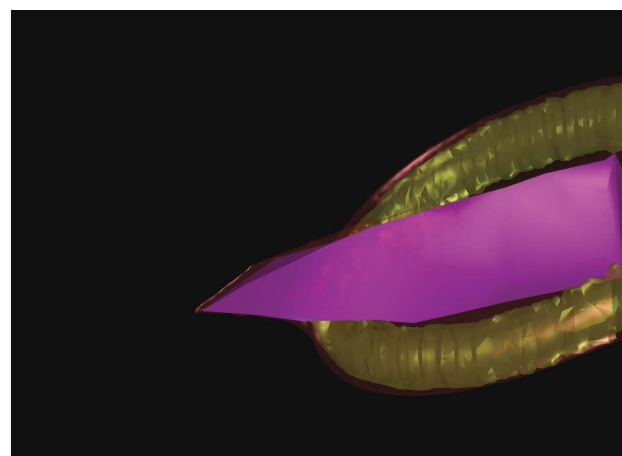

(a)

(b)

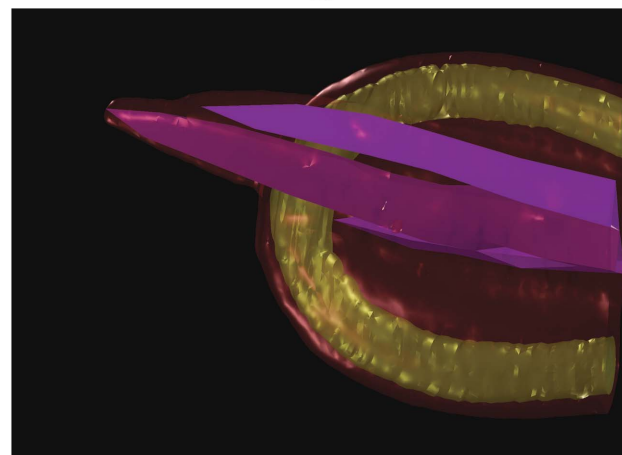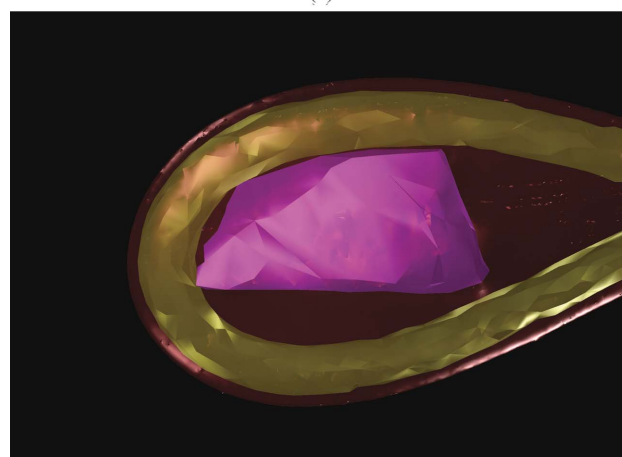**Figure 7**
Reconstructed two-dimensional tomograms of the native (a) and the iodinated (b) DNA samples, showing multiple crystals for the native example and cracks for the iodinated crystal. These tomograms are obtained from a complete set of flatfield-corrected projection images, such as those displayed in Fig. 6.

manual input as the data quality did not allow accurate automated segmentation by the software packages used.

The doses used to record the tomographic data series on the MX beamline have been estimated using the program *RADDOSE* (Ravelli *et al.*, 2002; Murray *et al.*, 2004, 2005) on the basis of the characteristics of the crystal, beam flux, energy and profile. They are approximately 4×10^5, 5×10^5 and 7×10^5 Gy for the native, brominated and iodinated crystals, respectively.

5. Discussion and conclusions

X-ray microtomography can give access to three-dimensional information of vitrified biological crystalline material with spatial resolution down to the micrometre range. This information would allow an analytical evaluation of absorption-correction factors, taking into account separate contributions from the crystalline diffracting material as well as the absorbing sample holder and mother liquor. Popular scaling programs such as *SCALA* (Evans, 2006), *SCALEPACK* (Otwinowski *et al.*, 2003) and *XSCALE* (Kabsch, 1988) use empirical correction schemes that rely on highly redundant data unaffected by systematic errors such as radiation damage. These have been highly optimized and are used routinely nowadays, although careful manual tuning can still be mandatory (Mueller-Dieckmann *et al.*, 2004). Owing to correlations between absorption-correction components and other components (Evans, 2006; Otwinowski *et al.*, 2003), we feel optimistic that calculated absorption factors could provide very useful restraints or constraints, especially when highly redundant data are not available. The benefits are also easily envisaged in the presence of radiation damage. The latter is reported to be the main course of failed MAD experiments at powerful undulator beamlines (Ravelli & Garman, 2006), as global and specific structural changes alter diffraction intensities during the course of the data collection. Scaling programs can only poorly model these radiation-damage-induced changes, which tempts users to exploit other parameters, such as those for absorption correction, to artificially improve their data. We believe that absorption corrections that are restrained to measured absorption paths, together with better models to treat radiation damage, would help to overcome systematic errors in synchrotron MX data.

The tomographic data could be collected after the collection of the MX data. The geometry of the fragile crystalline biological sample is expected to remain unaltered with doses typically used in MX, provided it is maintained at a temperature well below the glass transition (Weik *et al.*, 2001, 2005). This data collection order would have the advantage that all of the limited crystalline diffraction lifetime of the sample would serve the MX data collection. However, our experiments on the MX beamline showed that a complete tomographic data set could be collected within a few percent of the Henderson (Henderson, 1990; Owen *et al.*, 2006) limit. A number of improvements could further reduce this dose. We used a 6 µm layer of LAG as an X-ray converter screen, which absorbs 32% of incoming 12.7 keV photons. A thicker layer could improve the efficiency significantly (*e.g.* 73% for a 24 µm layer), while the spatial resolution would remain adequate for our studies. The light collection efficiency could be improved by the use of higher numerical aperture lenses. Newer CCD cameras with improved quantum efficiency are already available. Last but not least, positional beam fluctuations on the MX beamline, although not detrimental for the diffraction experiment, did compromise the quality of the imaging data. Modern optical elements, currently being installed on ID14-4, could help to overcome these problems. Overall, it should be possible to obtain a complete microtomographic data set using well below 1% of the Henderson limit.

Such a low dose would allow the use of X-ray microtomography for routine crystal alignment. It would overcome limitations in currently used crystal-centring methods that are based on visible or UV light images, as implemented in programs such as *Xrec* (Pothineni *et al.*, 2006) and *C3D* (Lavault *et al.*, 2006). These programs are efficient in pre-aligning the sample holder and finding a single large crystal within the holder but are challenged when dealing with highly transparent crystals, bad cryocooling or lens effects. The use of undistorted X-ray projection images on a pre-aligned loop could greatly facilitate this process. The X-ray dose could be reduced by another two orders of magnitude if the crystal centring was based on just a small number of these projection images instead of a complete tomographic data set. As current crystal centring programs often include edge-finding algorithms, they will be particularly useful for X-ray radiographs with clear phase contrast.

Fig. 7 argues for the routine collection of complete tomographic data sets. Current data collection pipelines have no means of deciding whether a whole crystal should be used for data collection or just a part of it. Often, the latter is used given the fine focal spot size of modern beamlines. The pipeline is seen to be successful if any part of the crystal was irradiated by the beam, and the difficult task of determining whether another part of a crystal could give better data is left to human intervention. A three-dimensional tomographic reconstruction of the crystal would allow a perfect matching of the beamsize with the rotating crystal, as well as the identification of problematic (parts of) crystals. Ultimately, tomography could serve automated data collection on multiple microcrystals on a microfocus beamline (Coulibaly *et al.*, 2007; Arzt *et al.*, 2005), a process that is currently entirely manual, time consuming and cumbersome.

We have shown that the microtomography setup, routinely used for materials science on dedicated imaging synchrotron beamlines, can also be integrated within the tight environment of an MX beamline. However, a dedicated imaging beamline does offer some important advantages, in particular at lower energies (< 30 keV). The combination of high photon flux of the white or pink beam, very fast cameras and continuous rotation of the sample allows one to acquire a typical data set in 10–20 s (Di Michiel *et al.*, 2005). More importantly, all components of such a beamline are optimized to preserve phase coherence and beam uniformity over an area much larger than the crystal. The phase contrast can be of particular

research papers

importance for automatic segmentation of the tomogram into crystal *versus* the surrounding solvent, as these show very little difference in absorption contrast. Nevertheless, the tomographic data collected on the MX beamline also clearly showed phased contrast, calling for further studies that will try to exploit this, for example by holotomography (Cloetens *et al.*, 2006).

References

Alcock, N. W. (1970). *Acta Cryst.* A**26**, 437–439.
Alcock, N. W. (1974). *Acta Cryst.* A**30**, 332–335.
Alcock, N. W., Pawley, G. S., Rourke, C. P. & Levine, M. R. (1972). *Acta Cryst.* A**28**, 440–444.
Arndt, U. W. (1984). *J. Appl. Cryst.* **17**, 118–119.
Arzt, S. *et al.* (2005). *Prog. Biophys. Mol. Biol.* **89**, 124–152.
Beteva, A. *et al.* (2006). *Acta Cryst.* D**62**, 1162–1169.
Blessing, R. H. (1995). *Acta Cryst.* A**51**, 33–38.
Cipriani, F. *et al.* (2006). *Acta Cryst.* D**62**, 1251–1259.
Clark, R. C. (1993). *Acta Cryst.* A**49**, 692–697.
Cloetens, P. (1999). PhD thesis, Vrije Universiteit Brussel, Belgium.
Cloetens, P., Mache, R., Schlenker, M. & Lerbs-Mache, S. (2006). *Proc. Natl Acad. Sci. USA*, **103**, 14626–14630.
Coppens, P., Leiserowitz, L. & Rabinovich, D. (1965). *Acta Cryst.* **18**, 1035–1038.
Coulibaly, F., Chiu, E., Ikeda, K., Gutmann, S., Haebel, P. W., Schulze-Briese, C., Mori, H. & Metcalf, P. (2007). *Nature* (*London*), **446**, 97–101.
DeTitta, G. T. (1985). *J. Appl. Cryst.* **18**, 75–79.
Di Michiel, M., Manuel, M. J., Fernandez-Carreiras, D., Buslaps, T., Honkimaki, V., Falus, P., Martins, T. & Svensson, O. (2005). *Rev. Sci. Instrum.* **76**, 1–7.
Evans, P. (2006). *Acta Cryst.* D**62**, 72–82.
Flack, H. D. (1974). *Acta Cryst.* A**30**, 569–573.
Flack, H. D. (1975). *J. Appl. Cryst.* **8**, 520–521.
Helliwell, J. R., Moore, P. R., Papiz, M. Z. & Smith, J. M. A. (1984). *J. Appl. Cryst.* **17**, 417–419.
Henderson, R. (1990). *Proc. R. Soc. London Ser. B*, **248**, 6–8.
Huber, R. & Kopfmann, G. (1969). *Acta Cryst.* A**25**, 143–152.
Izumi, T., Tsuruta, K., Fujitsuka, A., Kuchiji, H. & Kurihama, T. (1996). *J. Appl. Cryst.* **29**, 435–437.
Jakoncic, J., Di Michiel, M., Zhong, Z., Honkimaki, V., Jouanneau, Y. & Stojanoff, V. (2006). *J. Appl. Cryst.* **39**, 831–841.

Kabsch, W. (1988). *J. Appl. Cryst.* **21**, 916–924.
Kak, A. C. & Slaney, M. (1988). *Principles of Computerized Tomographic Imaging.* New York: IEEE Press.
Kopfmann, G. & Huber, R. (1968). *Acta Cryst.* A**24**, 348–351.
Langan, P., Forsyth, V. T. & Mahendrasingam, A. (1995). *J. Appl. Cryst.* **28**, 49–52.
Lavault, B., Ravelli, R. B. G. & Cipriani, F. (2006). *Acta Cryst.* D**62**, 1348–1357.
McGeehan, J. E., Carpentier, P., Royant, A., Bourgeois, D. & Ravelli, R. B. G. (2007). *J. Synchrotron Rad.* **14**, 99–108.
Messerschmidt, A., Schneider, M. & Huber, R. (1990). *J. Appl. Cryst.* **23**, 436–439.
Mueller-Dieckmann, C., Polentarutti, M., Djinovic Carugo, K., Panjikar, S., Tucker, P. A. & Weiss, M. S. (2004). *Acta Cryst.* D**60**, 28–38.
Murray, J. W., Garman, E. F. & Ravelli, R. B. G. (2004). *J. Appl. Cryst.* **37**, 513–522.
Murray, J. W., Rudiño-Piñera, E., Owen, R. L., Grininger, M., Ravelli, R. B. G. & Garman, E. F. (2005). *J. Synchrotron Rad.* **12**, 268–275.
North, A. C. T., Phillips, D. C. & Mathews, F. S. (1968). *Acta Cryst.* A**24**, 351–359.
Otwinowski, Z., Borek, D., Majewski, W. & Minor, W. (2003). *Acta Cryst.* A**59**, 228–234.
Owen, R. L., Rudino-Pinera, E. & Garman, E. F. (2006). *Proc. Natl Acad. Sci. USA*, **103**, 4912–4917.
Parkin, S., Moezzi, B. & Hope, H. (1995). *J. Appl. Cryst.* **28**, 53–56.
Pothineni, S. B., Strutz, T. & Lamzin, V. S. (2006). *Acta Cryst.* D**62**, 1358–1368.
Radon, J. (1917). *Ber. Verh. Sächs. Akad. Wiss.* (*Leipzig*), **69**, 262–277.
Ravelli, R. B. G. & Garman, E. F. (2006). *Curr. Opin. Struct. Biol.* **16**, 624–629.
Ravelli, R. B. G. & McSweeney, S. M. (2000). *Struct. Fold Des.* **8**, 315–328.
Ravelli, R. B. G., Theveneau, P., McSweeney, S. & Caffrey, M. (2002). *J. Synchrotron Rad.* **9**, 355–360.
Schwarzenbach, D. & Flack, H. D. (1989). *J. Appl. Cryst.* **22**, 601–605.
Sheldrick, G. M. (1996). *SADABS.* University of Göttingen, Germany.
Stuart, D. & Walker, N. (1979). *Acta Cryst.* A**35**, 925–933.
Tichý, K. (1970). *J. Appl. Cryst.* **3**, 542–543.
Walker, N. & Stuart, D. (1983). *Acta Cryst.* A**39**, 158–166.
Wang, J., Dauter, M. & Dauter, Z. (2006). *Acta Cryst.* D**62**, 1475–1483.
Ward, D. L. & Caughlan, C. N. (1971). *J. Appl. Cryst.* **4**, 400–401.
Weik, M., Kryger, G., Schreurs, A. M. M., Bouma, B., Silman, I., Sussman, J. L., Gros, P. & Kroon, J. (2001). *Acta Cryst.* D**57**, 566–573.
Weik, M., Ravelli, R. B. G., Kryger, G., McSweeney, S., Raves, M. L., Harel, M., Gros, P., Silman, I., Kroon, J. & Sussman, J. L. (2000). *Proc. Natl Acad. Sci. USA*, **97**, 623–628.
Weik, M., Schreurs, A. M. M., Leiros, H.-K. S., Zaccai, G., Ravelli, R. B. G. & Gros, P. (2005). *J. Synchrotron Rad.* **12**, 310–317.
Weitkamp, T. (2002). PhD thesis, Universitat Hamburg, Germany.